



Deterioration mechanism of chloride attack on reinforced concrete under stray current and high hydraulic pressure coexistence environment

Yongqing Chen · Mingyue Chen · Renpeng Chen · Xin Kang

Received: 1 April 2023 / Accepted: 17 August 2023 / Published online: 11 October 2023
© The Author(s), under exclusive licence to RILEM 2023

Abstract The evaluation method of chloride diffusion and the deterioration mechanism of reinforced concrete (RC) under the coexistent environment of high hydraulic pressure and stray current are essential for the development of ultra-deep underground rail transit projects in coastal cities. In this study, an advanced test system was developed to solve these urgent problems. The instantaneous electric conductivity during the entire deterioration process was continuously monitored. The microstructure of pores, the physical and mechanical properties of the interface transition zone (ITZ) between corroded reinforcement and concrete, and the pullout resistance of the

deteriorated specimens were comprehensively analyzed. The results showed that the instantaneous electric conductivity of specimens in ultra-deep buried environments depended on the distribution of free ions in concrete. Furthermore, the diffusion of chloride ions could be detected. Based on FTIR (Fourier transform infrared spectroscopy), Vickers hardness, and CT (computer tomography) scanning, the mechanism of bond deterioration between corroded reinforcement and concrete was revealed. These research results can provide a reference for the construction in ultra-deep underground rail transit projects.

Keywords Reinforced concrete · Stray current · Chloride induced corrosion · Instantaneous electrical conductivity · Microstructure characteristics · Diffusion coefficient

Y. Chen
School of Transportation Engineering, East China
Jiaotong University, Nanchang 330013, China

Y. Chen · M. Chen · R. Chen (✉) · X. Kang (✉)
College of Civil Engineering, Hunan University,
Changsha 410082, China
e-mail: chenrp@hnu.edu.cn

X. Kang
e-mail: kangxin@hnu.edu.cn

M. Chen · R. Chen · X. Kang
Key Laboratory of Building Safety and Energy Efficiency
of Ministry of Education, Hunan University,
Changsha 410082, China

M. Chen · R. Chen · X. Kang
National Center for International Research Collaboration
in Building Safety and Environment, Hunan University,
Changsha 410082, China

1 Introduction

Infrastructure in coastal cities is generally affected by chloride induced corrosion [1, 2]. The concentration of chloride ions is often higher in marine environments than in inland areas, making the impact of corrosion more significant. Coastal groundwater can be impacted by chloride ions, which may infiltrate the groundwater system from seawater. Additionally, chloride ions generated by sea fog and sea breeze



can also enter the underground environment via rainfall [3, 4]. High concentration of chloride ions in the underground environment [5, 6] (see Fig. 1a, b) will pose a great threat to the operation safety of utility

pipelines and underground infrastructure (such as tunnels, subway stations and building basements).

Rail transit is an important part of underground infrastructure, and stray current leakage is a frequent occurrence in direct current (DC) rail transit systems

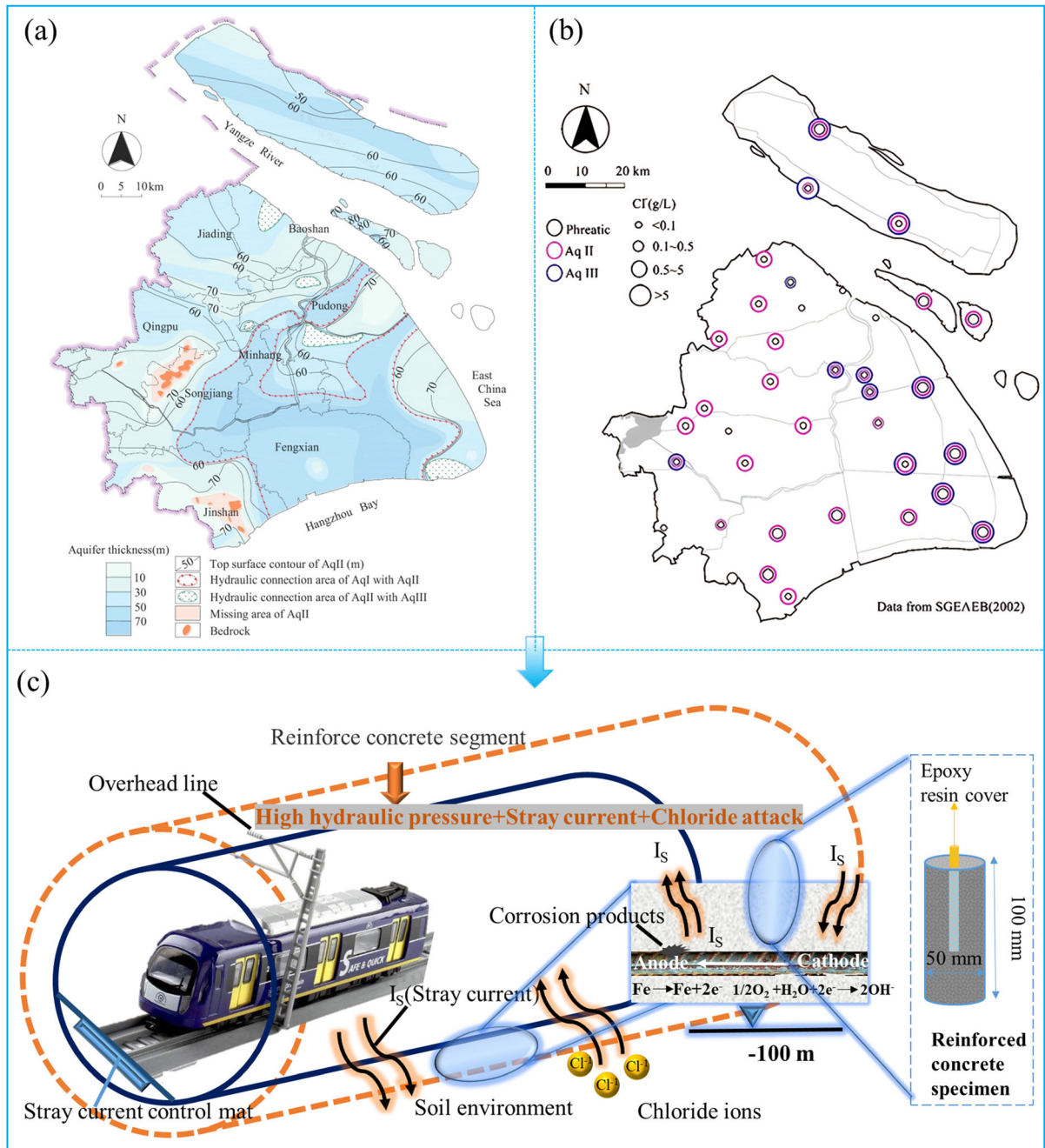


Fig. 1 The corrosive environment faced by the development of ultra-deep underground rail transit. **a** chlorides distribution of aquifers in Shanghai [5], **b** distribution of AqII in Shanghai [6], **c** the correlation between representative units and shield tunnel segments

[7, 8]. Grounding insulation is the primary means of controlling stray current, but when the insulation fails, stray current can flow into the underground environment through RC segments. This can be harmful to the tunnel's durability since stray current increases the influx of ions and leads to electrochemical corrosion [9]. On the one hand, the stray current makes the reinforcement undergo oxidation–reduction reaction. On the other hand, in some environments with electrochemical reactivity, such as seawater or ground water, stray current will greatly accelerate the migration of ions, thus accelerating the corrosion of reinforcement [10–12].

Ca leaching can cause a decrease in the strength and durability of concrete, among other detrimental effects. It can also result in the formation of pores and cracks within the concrete matrix, reducing its load-bearing capacity and resistance to corrosion [13]. Ca leaching will be more serious in the environment that is conducive to ion migration, such as immersion in soft water or electromigration [14, 15].

The aforementioned researches [10–12] have demonstrated that the presence of stray current and chloride can exert deleterious effects on the durability of reinforced concrete. Additionally, Ca leaching is also a common form of destruction. Our investigation stemmed from the State Major Program of National Natural Science Foundation of China–*Basic theory for resilience of deep underground space in megacities*, which aims to develop deep underground space (40 m–100 m) in coastal megalopolises. Up to now, coastal projects are mainly concentrated in the surface or shallow layer, and there is little corrosion study on the deterioration factors of reinforced concrete when all the above corrosion factors coexist. The development of rail transit projects in coastal ultra-deep underground spaces will face huge durability challenges (see Fig. 1c). The ultra-deep buried rail transit in coastal cities is still in its infancy. Previous studies have not considered chloride induced corrosion under stray current and high hydraulic pressure coexistence environment, which has brought huge potential safety hazards. Although the microstructure evolution of concrete and the molecular mechanism of chloride migration under this service environment have been revealed [16, 17], there remain numerous issues that must be addressed. It is critical to establish an evaluation method to monitor the diffusion of chloride and reveal the mechanism of bond deterioration

between corroded reinforcement and concrete to ensure the safety and durability of such deeply buried coastal infrastructure. To tackle this challenge, an advanced testing system was developed and a series of deterioration tests of reinforced concrete specimens were conducted. The instantaneous electric conductivity during the entire deterioration process was continuously monitored. The microstructure of the concrete, the physical and mechanical properties about interface transition zone (ITZ), and the pullout resistance of the deteriorated specimens were comprehensively analyzed. The results indicated that the instantaneous electric conductivity of concrete samples in a saturated environment was related to the number and distribution of free ions inside. Based on FTIR, Vickers hardness, and CT scanning, the mechanism of bond deterioration between corroded reinforcement and concrete was revealed, and a bond-slip prediction model was established. This study lays a foundation for the development of reinforced concrete structures for ultra deep underground rail transit in coastal cities.

2 Materials and test setup

2.1 Materials

ASTM (American Society of Testing Materials) Type I Portland cement (CEM I 42.5) was used in this study, and its chemical composition was evaluated to determine the hydration products [16]. Representative units (see Fig. 1c) inside the shield tunnel segment were used to study the mechanism of ultra-deep environmental corrosion degradation. For the actual size of the segments (generally greater than 500 mm in thickness, and thicker for ultra-deep underground rail transit projects), it could still be considered uniform after adding coarse aggregate. However, for the sample size in laboratory, coarse aggregate had a significant impact because the diameter of specimens in our specimens was 50 mm. Both (concrete in the shield tunnel segment structure and laboratory specimens) were considered uniform within their respective scale ranges. Therefore, the deterioration mechanism explored through specimens have guiding significance for the design of future deep buried segments. To avoid the influence of uneven distribution of coarse aggregates on the specimens, only fine

aggregates were added. The superplasticizer (Polyhydroxy acid high performance water reducer) was added into the slurry, and its effective dosage was 0.2% of the mass of cement. The samples were demoulded after 24 h, and cured in the standard curing box (with a relative humidity of 95% and a temperature of 20 ± 2 °C) for 28 days. The specific dimensions of the developed mould and specimen are shown in Fig. 2a–c.

2.2 Ultra-deep underground corrosion simulation system

A specialized test apparatus was developed by modifying our original test device [16] to add corrosion testing capabilities of reinforced concrete specimens (see Fig. 2d). The developed test apparatus is based on our original equipment for studying ultra-deep underground environments [16] and adds an instantaneous conductivity testing circuit and a corrosion testing box for reinforced concrete specimens. The photo of the experimental setup was shown in Fig. 2e, where each component can be identified. The factorial test design was adopted to study the corrosion process. The stray current densities and the hydraulic pressure became the factor points of the orthogonal experiment, the cement pastes in concrete were mixed at water to cement (W/P) ratio of 0.34, the stray current densities and hydraulic pressure varied, respectively, from 0.5 to 1.5 A/m² and from 0.4 to 1.0 MPa. More details of the factorial test design can be found in Table 1. The precise stray current was achieved through the constant current function of the power supply, and the loading of hydraulic pressure was provided by an air pressure pump, which was further regulated by a precision regulating valve. In this simulated environment, the corrosion solution was 10% NaCl and the anode solution was 0.3 mol/l NaOH. All samples were corroded for 28 days.

3 Test methods

3.1 The instantaneous electrical conductivity

The instantaneous electrical conductivity of RC was measured to obtain the evolution law of its ability to transmit current (see Fig. 3). The instantaneous electrical flux of corroded RC was recorded every 8 h

through a multi-function electrical indicator tester (see Fig. 2d). The instantaneous electrical conductivity σ was computed using Ohm's law from voltage V and current passed I as follows.

$$\sigma = \frac{1}{\rho} = \frac{IL}{VA} = \frac{L}{RA} \quad (1)$$

where A is the surface area, L is the length of the specimen and R is the bulk resistance. The circuit connection is shown by the red solid line, and the photo of the electrode plate is shown in the upper left of Fig. 2d.

3.2 Nitrogen adsorption

The pore size distribution and pore connectivity of internal microstructure in concrete were obtained through nitrogen adsorption test. SEM allowed direct observation, but it was a qualitative method [18] (see Fig. 4a). It was necessary to reveal the microstructure characteristics of deteriorated concrete by quantitative means (see Fig. 4). The low-temperature N₂ adsorption method did not damage the pore structures during the measurement process, and has the advantages of wide measuring range and low cost. At the same time, the adsorption isotherm curves could reflect the range and distribution of pore diameter, pore volume, and these curves could also reveal the information of pore shapes, especially for the characterization of “ink-bottle” type pores. According to our previous research [16], although nitrogen adsorption cannot reflect the distribution of macropores, the evolution law of porosity and critical pores diameters measured by nitrogen are consistent with MIP (mercury intrusion porosimetry) test.

In this study, the Tristar II 3flex surface area and porosity analyzer was employed to conduct low-temperature nitrogen adsorption experiments. Firstly, samples with particle size of approximately 0.5 mm and a depth of about 1 mm from the contact surface with the solution were subjected to 24 h of vacuum degassing treatment in a vacuum drying oven at 40 °C and a vacuum degree of 0.06 MPa. Then, a sample weighing approximately 1.0 g was taken, and high-purity nitrogen with a purity of over 99.999% was used as the adsorbate. The adsorption/desorption isotherm curves were plotted using the relative pressure p/p_0 as the abscissa and the adsorption capacity as the ordinate. The specific surface area and total pore



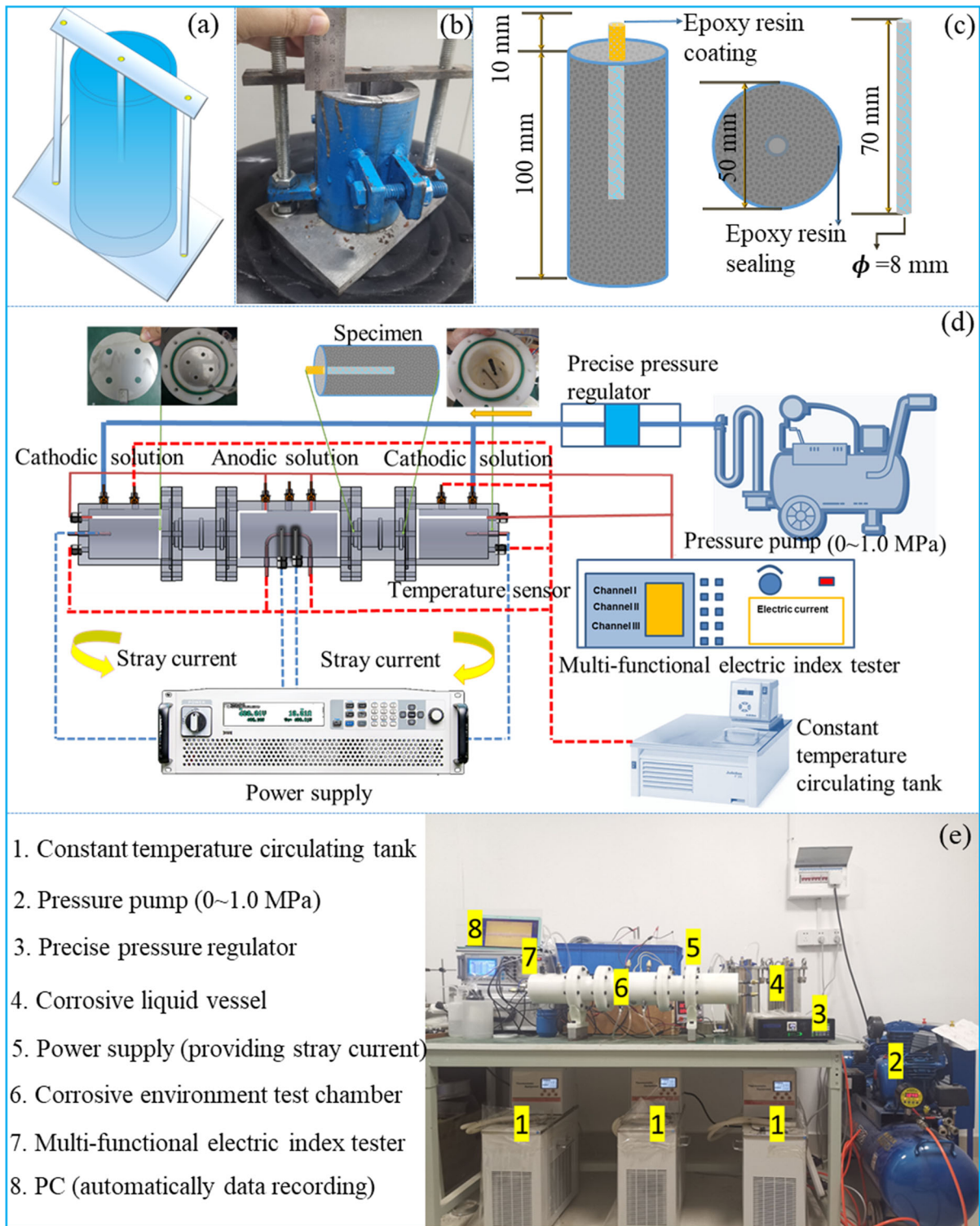


Fig. 2 Ultra-deep underground corrosion simulation system. **a** schematic diagram of the recently designed and developed mould, **b** a photo of developed mould, **c** schematic diagram of

concrete specimen (epoxy resin applied on the side of concrete and exposed reinforcement), **d** schematic view of the experimental system, **e** a photo of the experimental setup

Table 1 Test samples of factorial experiment design

Order no.	Cement (kg/m ³)	Aggregates (kg/m ³)	Electric current density (A/m ²)	Water (kg/m ³)	Water pressure (MPa)	W/C (%)	Sample no.
1	650	1530	0	221	0.4	0.34	S1
2	650	1530	0	221	0.7	0.34	S2
3	650	1530	0	221	1.0	0.34	S3
4	650	1530	0.5	221	0.4	0.34	S4
5	650	1530	0.5	221	0.7	0.34	S5
6	650	1530	0.5	221	1.0	0.34	S6
7	650	1530	1.0	221	0.4	0.34	S7
8	650	1530	1.0	221	0.7	0.34	S8
9	650	1530	1.0	221	1.0	0.34	S9
10	650	1530	1.5	221	0.4	0.34	S10
11	650	1530	1.5	221	0.7	0.34	S11
12	650	1530	1.5	221	1.0	0.34	S12

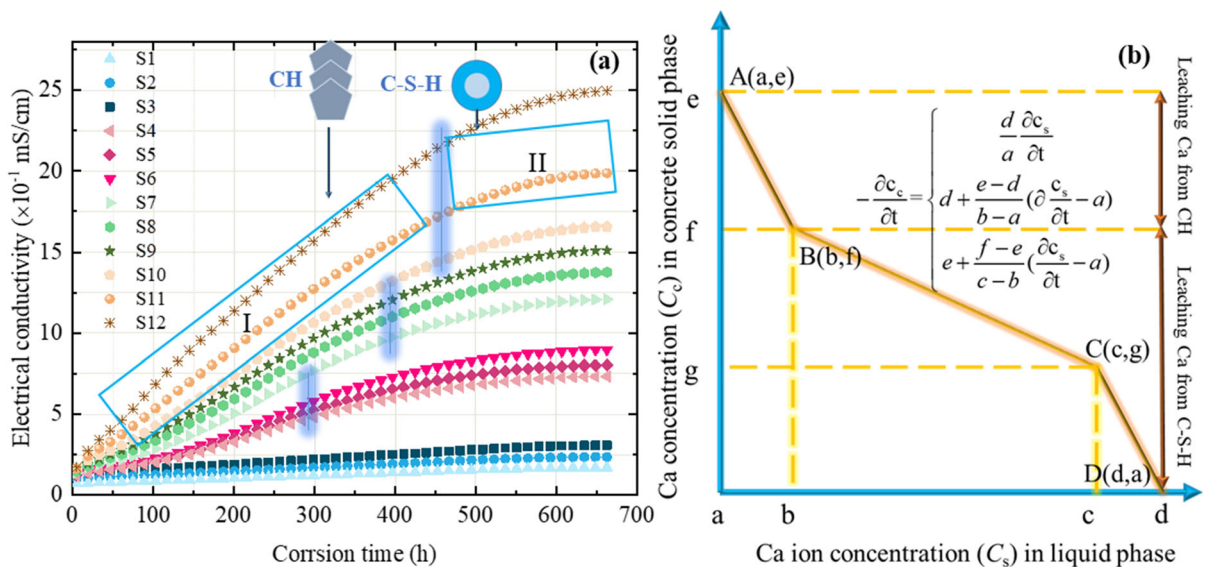


Fig. 3 The evolution of instantaneous electric conductivity and electrochemical decomposition during corrosion. **a** the instantaneous electric conductivity versus corrosion time, **b** Ca concentration (C_s) in concrete solid phase versus Ca ion concentration (C_l) in the liquid phase (AB segment: in the region of $a \leq C_s \leq b$, the dissolved Ca concentration (C_s)

between a and b corresponds to the dissolution of CH; BC segment: in the region of $b \leq C_s \leq c$, C-S-H begins to be progressively dissolved; CD segment: the region $c \leq C_s \leq d$ corresponds to a quicker decalcification of C-S-H to form silica gel)

volume of the samples were calculated using the BET (Brunauer–Emmett–Teller method) equation, with the adsorption branch serving as the data source. The desorption branch was used as the data source to calculate the aperture distribution via the Kelvin

equation and the BJH (Barret-Joyner-Halenda) model [19].



3.3 Vickers hardness

HV-10 digital microhardness tester was used to obtain the Vickers hardness of concrete samples on the representative positions. The classical polishing procedure [20] was used to prepare samples for Vickers hardness test: In the first stage, Buehler's (Lake Bluff, USA) IsoMet diamond saw was used to cut samples from each specimen at the central positions of 10 mm, 30 mm, 50 mm from the bottom of the reinforcement (see Fig. 5a). Then each sample was installed on the AFM disk with Cyanoacrylate glue (Ted Pella, USA), and automatically ground in a specially designed system. TexMet P pad (Buehler, USA) and 9 μm MetaDi (Buehler, USA) were used for grinding the samples with oil-based diamond suspension. A typical grinding process lasted for a total of about 20 min, and was subjected to three 9-min ultrasonic treatments in isopropanol solution. Finally, the ground and cleaned samples were manually polished on a FibrMet (Lake Bluff, USA) alumina grinding disc with abrasive sizes of 9 μm , 3 μm , and 1 μm . The exchange of each pad was accompanied by cleaning the sample with isopropanol in an ultrasonic bath for 1 min. The main test parameters were as follows: the load was 0.9807 N, and the load holding time was 10 s. The Vickers hardness test was carried out by using the local micro characterization capability of the HV-10 digital microhardness tester. The resin inlaid samples were processed (see Fig. 5b), and the test positions were gradually moved from ITZ to cement matrix (see Fig. 5c). The Vickers hardness HV was calculated by Eq. (2) [21].

$$HV = \frac{P}{A} = \frac{2P \sin(\alpha/2)}{D^2} = \frac{1.854P}{D^2} \quad (2)$$

where P is the test force (kgf), α is the indenter diagonals angle, equals to 136° ; A and D is the area of indentation (mm^2) and the average of diagonals of indentation (mm), respectively.

3.4 Fourier transform infrared (FTIR) spectroscopy

FTIR has been proved to have extremely high accuracy in detecting the strength of functional groups and Chemical bond [22]. The FTIR spectra of concrete powder samples were collected in transmission mode by Shimadzu Europa IRAffinity-1S FTIR

spectrometer (see Fig. 6). Sample pallets were prepared by mixing 250 mg of potassium bromide (KBr) with 3 mg of concrete powder samples. The detailed process of powder preparation is as follows: first, the specimens were half cylindrical, the steel bars were carefully removed, and then the corroded steel products were cleaned. Finally, the concrete powders at the ITZ position were ground using diamond sandpaper. Fifteen scans were recorded over a range of $4000\text{--}400\text{ cm}^{-1}$. The background spectrum was collected in ambient atmosphere with the instrument's scanning time set to 32 s and a resolution of 2 cm^{-1} . Subsequently, the spectra of the samples were collected.

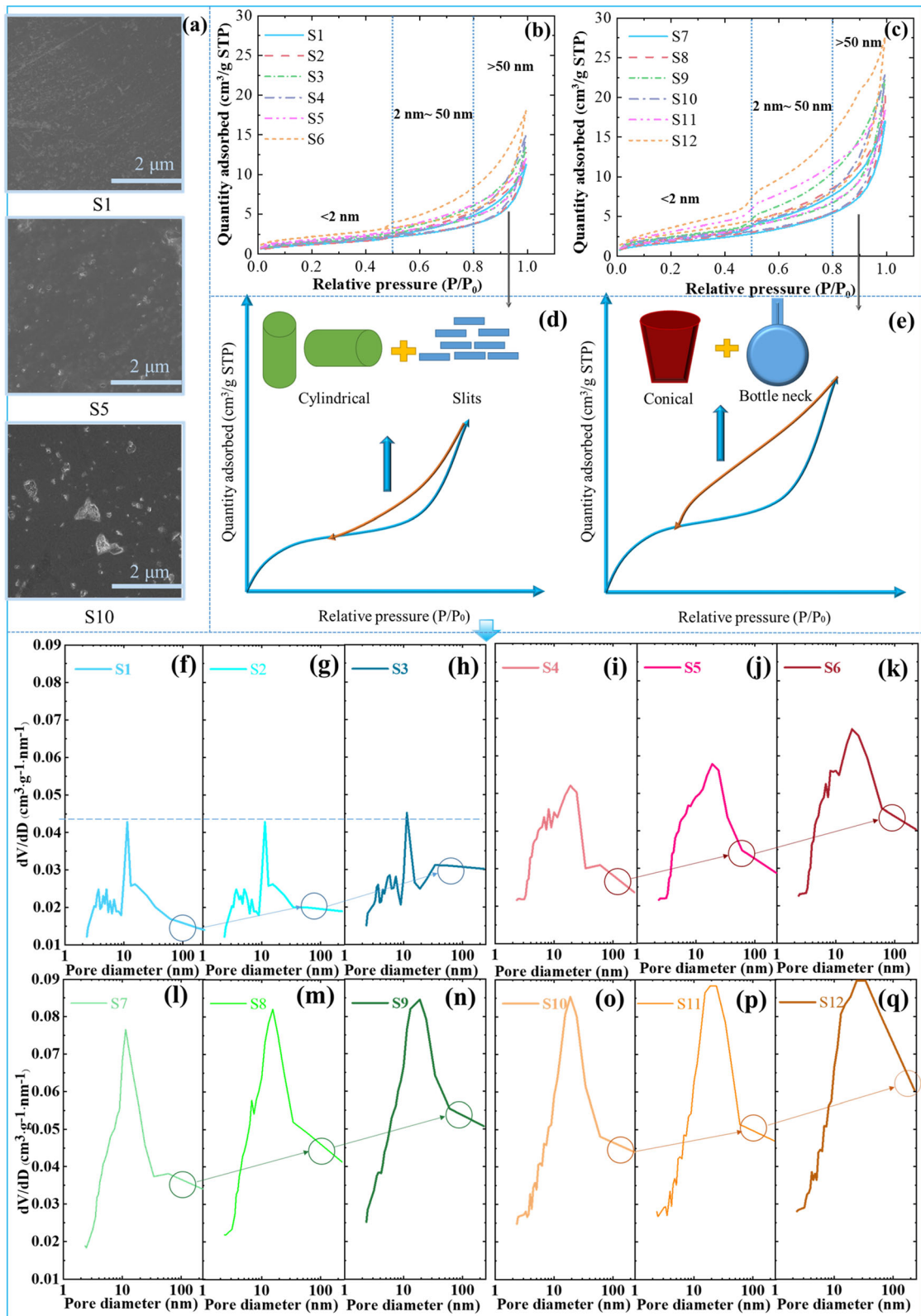
3.5 Computerized tomography

Micro-CT scans were conducted using a microXCT-400 X-ray microscope (Zeiss Xradia). Unlike other techniques, computerized tomography (CT scanning) does not require special sample processing such as spraying, cutting, or resin inlaying, making it a highly effective method for nondestructive detection of internal information in opaque objects (see Fig. 7). The scans were carried out at 60 kV (W target) and 150 μA with 1601 projections taken at an angle step of 0.225° from -180° to 180° and a 6 s exposure time per projection. A $10\times$ magnification optical objective was used to acquire the data, and the entire scan, including the collection of reference images, took 4 h in total (see Fig. 7). The CT scanning intuitively displayed the internal structure, composition and defect of RC in the form of two-dimensional section images or three-dimensional images without damage to the corroded RC specimens (see Fig. 7b). The total volume of CT scanning voxels was $1854 \times 1964 \times 2000$, and the scanning results can be derived into 2000 layers of 1854×1964 pixels. The slices were 16-bit images with a gray value range of 0 to 65,535.

3.6 Pull-out test

The pull-out test can be used to evaluate the bonding ability between corroded reinforcement and concrete [22]. The bonding ability between corroded reinforcement and concrete is mainly attributed to three mechanisms: chemical adhesive force, friction resistance, and mechanical interlocking force. Chemical





◀ **Fig. 4** A comparison of the N₂ adsorption/desorption isotherms and pore diameter distribution of 28-day corroded samples. **a** SEM photos of representative samples, **b** the adsorption/desorption curves of S1–S6, **c** the adsorption/desorption curves of S7–S12, **d** the H3 type pores: including flat slit-shaped or plate-like structure, cracks and wedge-shaped structure, and there was no adsorption saturation in the area with high nitrogen relative pressure (appeared when stray current was relatively smaller), **e** the H2 type pores: with the increase of stray current, the pore structures of H3 type gradually changed into typical ink-bottle-shaped pores, tubular pores with uneven pores size distribution, and closely packed spherical particle gap pores. Pore diameter distribution of 28-day corroded samples: **f** S1, **g** S2, **h** S3, **i** S4, **j** S5, **k** S6, **l** S7, **m** S8, **n** S9, **o** S10, **p** S11, **q** S12

adhesive force is generated by the cement gel of concrete on the surface of reinforcement. Friction resistance and mechanical interlocking force result from the unevenness of the steel bar surface, where the longitudinal and transverse ribs of the steel bar surface are embedded in the concrete to form a certain friction

and mechanical interlocking effect. These three forces are related to the roughness and degree of corrosion of the reinforcement surface and concrete.

Pull-out tests were performed on 12 specimens via a universal testing machine. The forces were measured by a 20t load sensor, and the slip values were recorded using a displacement sensor. The loading process is illustrated in Fig. 8a. To ensure that the slip values were caused by the drawing of the reinforcement bars, a rigid fixture was designed for the universal testing machine (as shown in Fig. 8b). The pull-out test set-up was conducted in accordance with the specifications of ASTM C-234-91a, and was performed with a stiff test frame at a loading rate of 0.01 mm/s under displacement control.

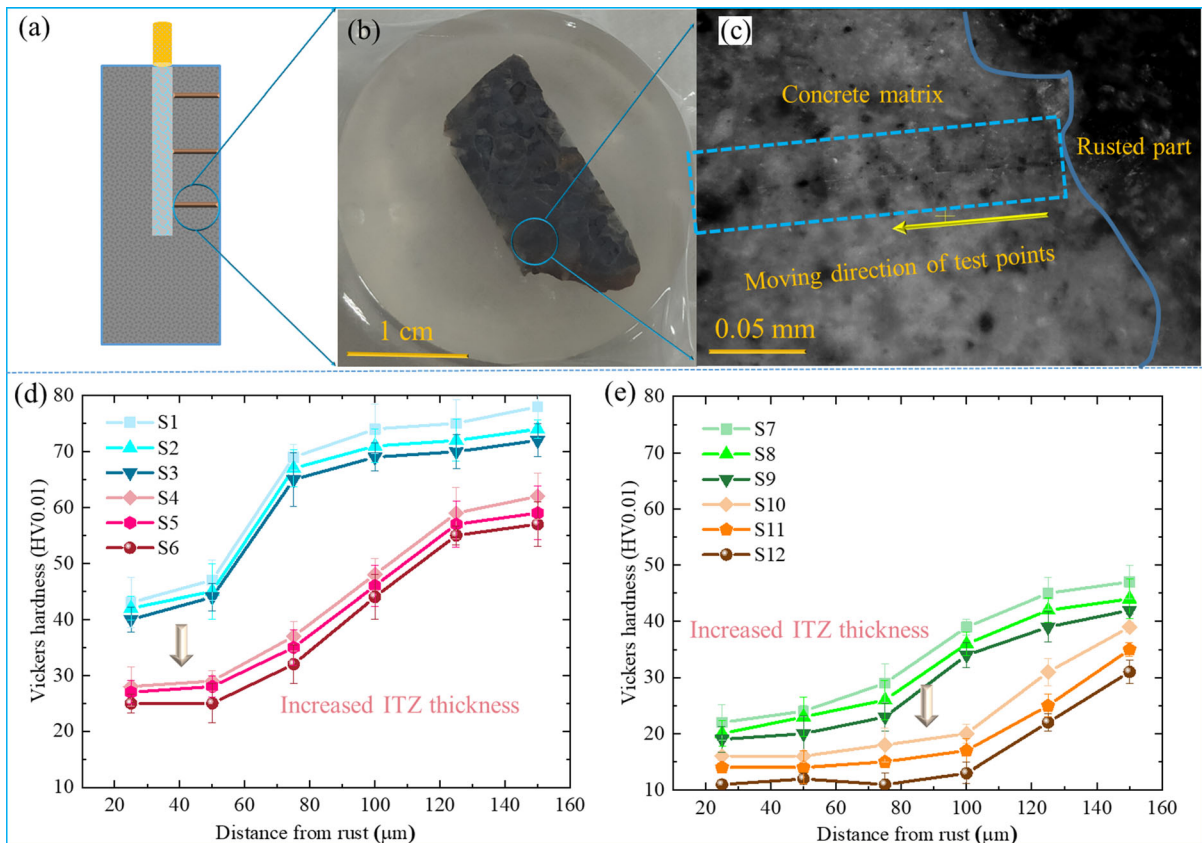


Fig. 5 Vickers hardness of ITZ in 28-day corroded samples. **a** schematic diagram of sampling location, **b** a photo of resin-inlaid sample, **c** test points of Vickers hardness, **d** and **e** Vickers hardness distribution at different locations

4 Results and discussions

4.1 Electric conductivity evolution during deterioration

The relationship between electric conductivity and corrosion time can be seen in Fig. 3a. When the specimens were installed into the simulated corrosion test system, the chloride ion solution and sodium hydroxide solution were added immediately, and the high hydraulic pressure and stray current were loaded at the same time. This time was considered as the starting time of the corrosion. The evolution law of electrical conductivity was very consistent with the first two stages of calcium leaching theory of cement-based composites [23, 24], and can be roughly divided into two stages (see Fig. 3a). The first stage mainly corresponds to the decomposition of CaOH (calcium hydroxide), Ca leaching at this stage was considered to be significantly faster. The second stage mainly corresponds to the decomposition of C-S-H (calcium silicate hydrate). The conductivity increased more slowly in the second stage due to the slower decomposition rate of C-S-H (see Fig. 3b). The electro-chemical decomposition process is shown in Eq. (3).

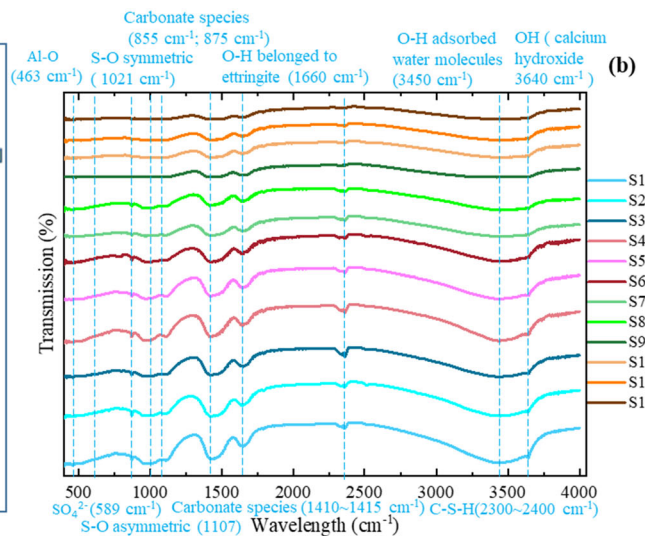
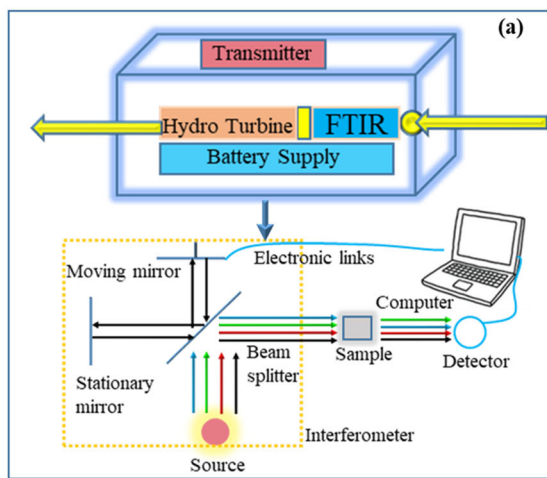
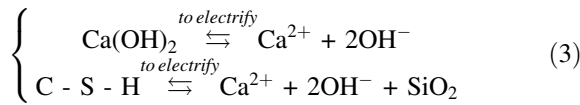
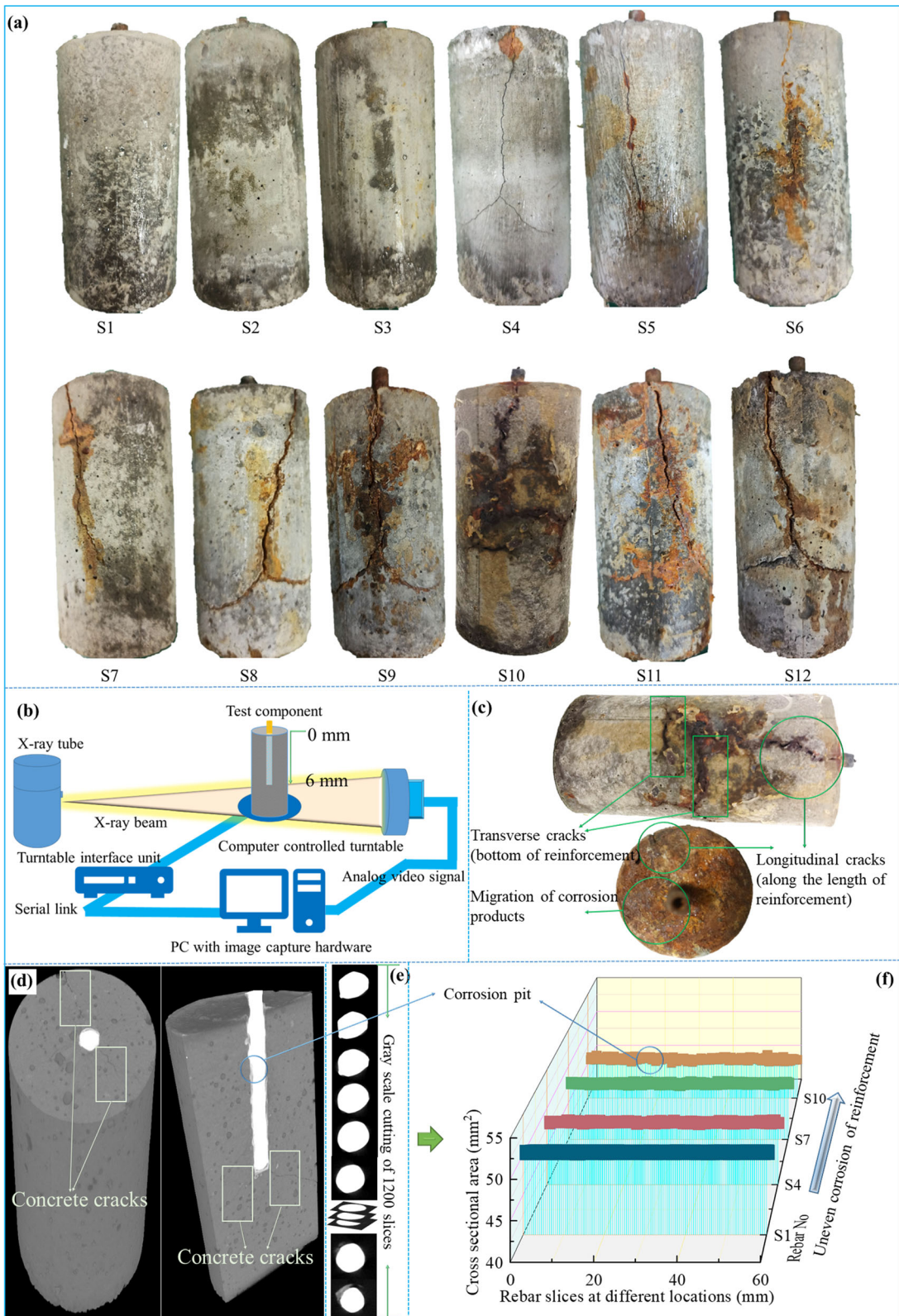


Fig. 6 The FTIR spectra of paste matrix in ITZ and the evolution of functional groups and chemical bonds. **a** transmission mode of FTIR, **b** functional groups and chemical bonds of ITZ in samples S1–S12



Fig. 7 The morphology of the reinforced concrete specimens after the deterioration of the designed test procedure. **a** photos of specimens corroded for 28 days, **b** the test process of CT scanning, **c** photos of representative sample S10 after 28-day corrosion, **d** the CT scanning results (the gray values of each phase from small to large were: pores, mortar, corrosion products and reinforcement bars), **e** the rebar contour of 1200 slices, **f** the cross-sectional area evolution and morphology of the reconstructed reinforcement after pixel-level segmentation

The electrical conductivity was considered to be closely related to the leaching of calcium and the intrusion of chloride. Ca leaching was a decompose process of the cement matrix, and then formed more pores. The increase of porosity also made the chloride solution contact more fresh cement matrix. The cracks caused by the expansion of corroded steel bars also increased the migration path of free ions. These processes increased the number of ions in the pore solution, and further enhanced the electric conductivity of concrete. A faster decomposition rate for the cement-based composites occurred under stronger stray currents. The hydraulic pressure could only work if the pores exceeded a certain size, which was consistent with our previous molecular dynamics simulation results [17]: when the nominal radius of hydrated ions was greater than the pore radius, the ions could not invade the corresponding nano pores. However, the stray current could destroy the



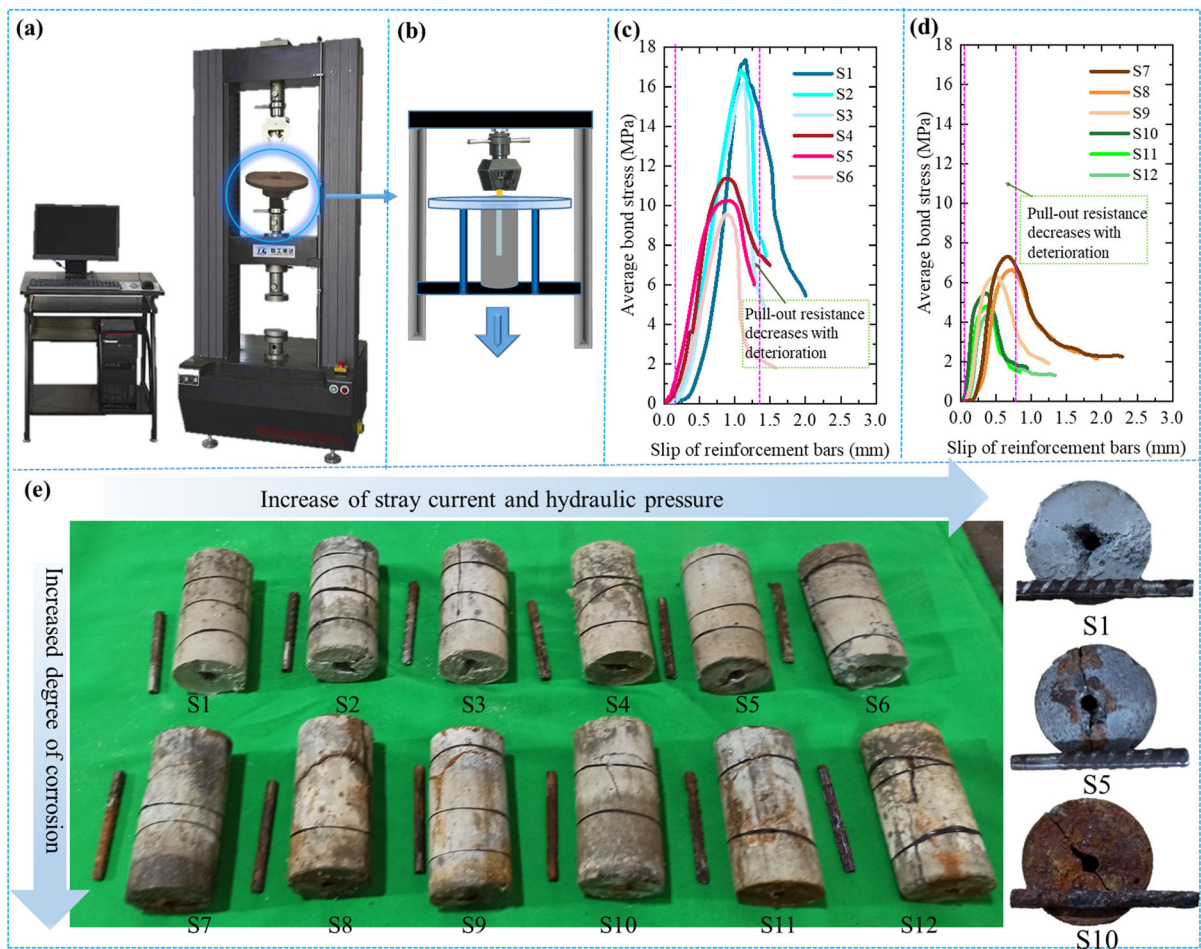


Fig. 8 The pull-out test and bond-slip curves. **a** the loading device, **b** the rigid fixture, **c** and **d** the average bond-slip curves of S1–S12, **e** the morphology of the specimens after the pull-out test

“hydration cage” and ion clusters, making chloride ions have stronger migration ability.

4.2 Pore structure evidence of electric conductivity evolution

The qualitative characteristics of pores could be seen in Fig. 4), the shape, connectivity and pore size distribution of pores were directly observed and analyzed by SEM images. Further, the quantitative indicators were collected by nitrogen adsorption [25]. It can be seen from Fig. 4b, c that the adsorption/desorption isotherm curves were generally in inverse “S” shapes, and showed hysteresis loops (see Fig. 4d, e). The hysteresis loops were due to the capillary condensation. When the stray current was relatively

smaller, the H3 type (named by International Union of Pure and Applied Chemistry) pores were displayed [25]: including flat slit-shaped or plate-like structure, cracks and wedge-shaped structure, and there was no adsorption saturation in the area with high nitrogen relative pressure (see Fig. 4d). With the increase of stray current, the pore structures of H3 type gradually changes into typical ink-bottle-shaped pores, tubular pores with uneven pores size distribution, that is, transformed into H2 type (named by International Union of Pure and Applied Chemistry) pores [25] (see Fig. 4e). Figure 4b, c demonstrate that the adsorption isotherm of the samples had significantly smaller slopes during the stage of relative pressure $p/p_0 < 0.5$, indicating slow monolayer adsorption and 0.5–2.0 nm micropore filling. As the relative pressure increased to

$0.5 < p/p_0 < 0.8$ and $0.8 < p/p_0 < 1.0$, the adsorption isotherm rose sharply, which corresponded to multi-layer adsorption of N_2 and capillary condensation in macropores. During these two stages, the adsorption curves formed distinct hysteresis loops with the desorption curves, indicating that the samples contained a considerable number of mesopores [25]. At the relative pressure $p/p_0 < 0.5$, the adsorption/desorption curves almost overlapped under the same stray current, indicating a negligible difference in the proportion of micropores in the samples. Nevertheless, higher stray current intensity resulted in a greater adsorption capacity within the range of $p/p_0 < 0.5$, suggesting more severe Ca leaching and an increased number of micropores. The hydraulic pressure mainly affected the macropores, as illustrated in Fig. 4f–q, where the proportion of macropores increased with the increased hydraulic pressure [26].

The pore structure parameters were calculated and presented in Table 2. The volume and specific surface area of micropores had almost no correlation with high hydraulic pressure, and the ratio of mesopores to micropores increased slightly when in a corrosive environment without stray current. However, when the stray current increased to 0.5 A/m^2 , the BET surface area, BJH adsorption average pore diameter, and total porosity increased to approximately twice that of the condition with no stray current. The specific surface area and volume of micropores increased to about four

and three times, respectively. The underlying mechanism behind this phenomenon was the electrochemical decomposition of calcium hydroxide and hydrated calcium silicate by the stray current. Additionally, the decomposition rate of calcium hydroxide was faster and earlier than that of calcium silicate hydrate. As a result, the micropores were preferentially exposed after the decomposition of calcium hydroxide, causing the growth rate of mesopores and macropores to be slower than that of micropores. Further designed tests of 1.0 A/m^2 and 1.5 A/m^2 supported this conclusion (see Table 2). Previous research has found that the front of phase decomposition was almost the same as the front of chloride migration [16]. Therefore, it could be inferred that the stray current filled the micropores with chloride solution, thus increasing the accessibility of chloride ions.

4.3 Mechanical properties of ITZ between corroded reinforcement and matrix

The thickness and mechanical properties of ITZ were indirectly evaluated by Vickers hardness test (see Fig. 5d, e). When the stray current increased, the ITZ thickness increased significantly. The effect of hydraulic pressure was not obvious, because the increase of hydraulic pressure mainly acted on macropores (see Sect. 4.2). Therefore, under the same stray current but different hydraulic conditions, the

Table 2 Influence of simulated ultra-deep buried underground environment on internal microstructure parameters of concrete

Sample no.	BET surface area (m^2/g)	BJH adsorption average pore diameter ((4 V/A) , nm)	Micropore spec. surface (m^2/g)	Micropore volume (mm^3/g)	Meso/micro volume ratio	Porosity (BJH) (%)
S1	13.9	15.1	5.4	7.5	5.4	6.1
S2	14.3	17.3	5.1	6.9	5.6	6.2
S3	14.4	18.8	5.4	7.2	5.8	6.4
S4	24.7	28.6	21.7	20.1	4.3	11.2
S5	28.6	30.2	23.1	23.7	4.5	12.6
S6	34.7	34.4	24.6	24.5	4.9	14.4
S7	95.5	27.9	32.7	32.4	3.7	17.1
S8	107.3	30.7	35.4	35.8	3.8	18.3
S9	121.4	35.0	38.4	39.0	4.3	19.3
S10	140.6	26.1	41.3	44.1	3.3	22.5
S11	158.2	31.7	44.9	46.6	3.6	24.4
S12	175.1	36.2	48.5	49.5	4.2	26.1

thickness of ITZ was roughly the same (see Fig. 5d, e). The thickness and microhardness of ITZ were very important for evaluating the bonding ability between reinforcement and concrete, because the mechanical biting force and friction depended on the strength of ITZ and the concrete nearby (see Sect. 4.6).

4.4 Evolution mechanism of chemical adhesion

The weakening of chemical adhesion was attributed to the electrochemical decomposition of hydration products, which was obtained through the analysis of chemical bonds and functional groups. After carefully removed the aggregates, the samples were dried in vacuum, then ground into powders and tested. The transmission mode was adopted (see Fig. 6a), and the FTIR spectra of paste matrix are shown in Fig. 6b. It can be seen from the Fig. 6b that the infrared Fourier had obvious absorption peaks in the wave number range of 3200–3600 cm^{-1} , which was mainly attributed to the vibration of –OH functional groups, including alkali metal bonded –OH (3640 cm^{-1}) and the tensile vibration of –OH in water molecules (the broadband centered on 3450 cm^{-1}) [27]. The –OH vibration of alkali metal could be inferred as calcium hydroxide, and the strength of its signal peak could be inferred as the content of calcium hydroxide. From the regular evolution of samples S1–S12 in Fig. 6b, it can be seen that the signal peak value of calcium hydroxide was obviously attenuated, indicated that stray current had obvious decomposition effect on calcium hydroxide. In addition, the vibration peak of bound water could characterize the content of hydrated calcium silicate to a certain extent, and the attenuation speed of its signal peak was slower than that of calcium hydroxide. Therefore, it could be inferred that the decomposition time of hydrated calcium silicate was later than that of calcium hydroxide. The different kinds of C–S–H vibration peaks at 2300–2400 cm^{-1} also verified this rule. In addition, they were oxygen-containing functional groups in the range of 1000–1800 cm^{-1} [28]. These groups had strong hydrophilicity, so they were often accompanied by vibration peaks of bound water. It can be seen from Fig. 6b that different samples also included S–O symmetric vibration band (1021 cm^{-1}) and S–O asymmetric vibration band (1107 cm^{-1}), as well as signal peaks of carbonate of different crystal types (1410 cm^{-1} –1415 cm^{-1}) [28, 29]. In addition,

the vibration band at 1660 cm^{-1} was due to –OH of belonged to ettringite [28, 30]. The low frequency area (400–1000 cm^{-1}) was called fingerprint area, the bands of 855 cm^{-1} and 875 cm^{-1} represented vibration peaks of different carbonates, while SO_4^{2-} vibration peaks appeared at 589 cm^{-1} . In addition, weak Al–O vibration peaks (463 cm^{-1}) were observed [28, 31]. Stray current significantly changed the functional groups and chemical bonds in concrete, while hydraulic pressure had little effect. These functional groups and chemical bonds were not only the source of the cementing force between aggregates and cement paste, but also the formation mechanism of the chemical bonding in ITZ between concrete and reinforcement surfaces.

4.5 Meso-scale contour modeling of corroded reinforcement

The photos of the RC specimens after the corrosion of the designed procedure are shown in Fig. 7a, and the evolution rule of appearance morphology of corroded RC can be obtained. When there was only high hydraulic pressure (S1–S3), the specimens did not show cracks after 28-day corrosion. When the stray current was 0.5 A/m^2 (S4–S6), there was slight cracks on the top surfaces and sides of the specimens. Rust was observed at the cracks (i.e. the vertical cracks along the reinforcement bars, and the transverse cracks perpendicular to the reinforcement bars). With the increase of hydraulic pressure but the same stray current (S4–S6), the change of fractures was not obvious. As the stray current increased to 1.0 A/m^2 and 1.5 A/m^2 (S6–S12), the development of cracks and the migration of rust were more obvious.

Sample S10 was taken as an example to describe the detailed process of meso-scale contour modeling. After 28-day chloride attack under the hydraulic pressure of 0.4 MPa coupled stray current of 1.5 A/m^2 , the photos of corroded S10 are shown in Fig. 7c. The CT scanning results of S10 are shown in Fig. 7d. The vertical cracks along reinforcement and the transverse cracks starting from the reinforcement bottom could be clearly observed. It could be inferred that both cracks were caused by tensile stress of rust expansion [32]. There was a significant gray difference between pores, mortar, corrosion products and reinforcement bars. The gray values of each phase from small to large were: pores, mortar, corrosion



products and reinforcement bars. The rebar contour of 1200 slices were divided by the threshold value, as shown in Fig. 7e. The reinforcement without any deterioration was used as the calibration of gray value, which was determined by the standard cross-sectional area, so as to accurately distinguished the reinforcement bars and corrosion products.

The cross-sectional area evolution and morphology of the reconstructed reinforcement are shown in Fig. 7f. The volume loss could be calculated as the amount of corrosion products of reinforcement. When the corrosion process was in the initial stage, the rust accumulated at the ITZ between the reinforcement and the concrete [33] or filled in the concrete pores outside the ITZ. When the corrosion of reinforcement exceeded a certain level, cracking of concrete caused by the oxidized rust products was observed [34]. It further provided a channel for the migration of corrosion products, so the rust distribution on the side and bottom surfaces of the specimens appeared (see Fig. 7c).

4.6 Evolution of bond-slip relationship

The average bond-slip curves can be seen in Fig. 8c, d, and the failure morphology of the specimens can be seen in Fig. 8e. The average bond strength is calculated as follows:

$$\bar{\tau} = \frac{P}{\pi dl} \quad (4)$$

where $\bar{\tau}$ is the average bonding stress (MPa); P is the pull-out load (N); d is the diameter of an equivalent circle equal to the cross-sectional area of reinforcement) (mm); l is the bonding length (mm).

It can be seen from Fig. 8 that the ultimate bond stress decreased with the increase of stray current and hydraulic pressure. The statistics of ultimate bond stress, ultimate peak slip and corrosion amount are shown in Table 3 (the ultimate slip value is the corrected value after removing the gap between the

specimens and the rigid frame that is not in close contact, see Sect. 5.2). It is worth mentioning that the amount of corrosion of steel bars was counted according to the threshold segmentation method described in Sect. 4.5.

5 General discussion

5.1 Can the instantaneous electric conductivity reflect microstructure characteristics and effective diffusion of chloride?

The part with reinforcement and the part without reinforcement could be regarded as a series connection (see Fig. 9a). Therefore, the electrical conductivity parameters were controlled by the concrete without reinforcement at the bottom. The evolution of pore structure of bottom concrete led to the change of electrical conductivity, and the bulk specimen conductivity was related to the pore solution conductivity (σ_0) and a pore structure factor, defined herein as the product of porosity (ϕ) and pore connectivity (β) as [35, 36]:

$$\sigma_{\text{eff}} = \sigma_0 \phi \beta \quad (5)$$

According to Eq. 5, the parameter formation factor F_f can be defined.

$$F_f = \frac{\sigma_0}{\sigma_{\text{eff}}} = \frac{1}{\phi \beta} \quad (6)$$

The migration of ions in concrete can be described by the Nernst–Planck equation [37].

$$J_{i,e} = -D_{i,e} \left(\frac{\partial c_i}{\partial x} + c_i \frac{z_i F}{RT} \frac{\partial U}{\partial x} + c_i \frac{\partial \ln(y_i)}{\partial x} \right) \quad (7)$$

where the flux $J_{i,e}$ of species i is function of the diffusion coefficient $D_{i,e}$ and contributions from three terms related to concentration diffusion, migration and non-ideal diffusion (c_i is the concentration, z_i the electrical charge, y_i the activity coefficient, U the

Table 3 Pull-out test results of representative specimens

Sample no.	Corrosion ratio (%)	Ultimate bond stress (MPa)	Ultimate slip value (mm)
S1	0.06	17.35	0.85
S4	2.47	11.37	0.77
S7	5.01	7.32	0.56
S10	7.75	5.46	0.35

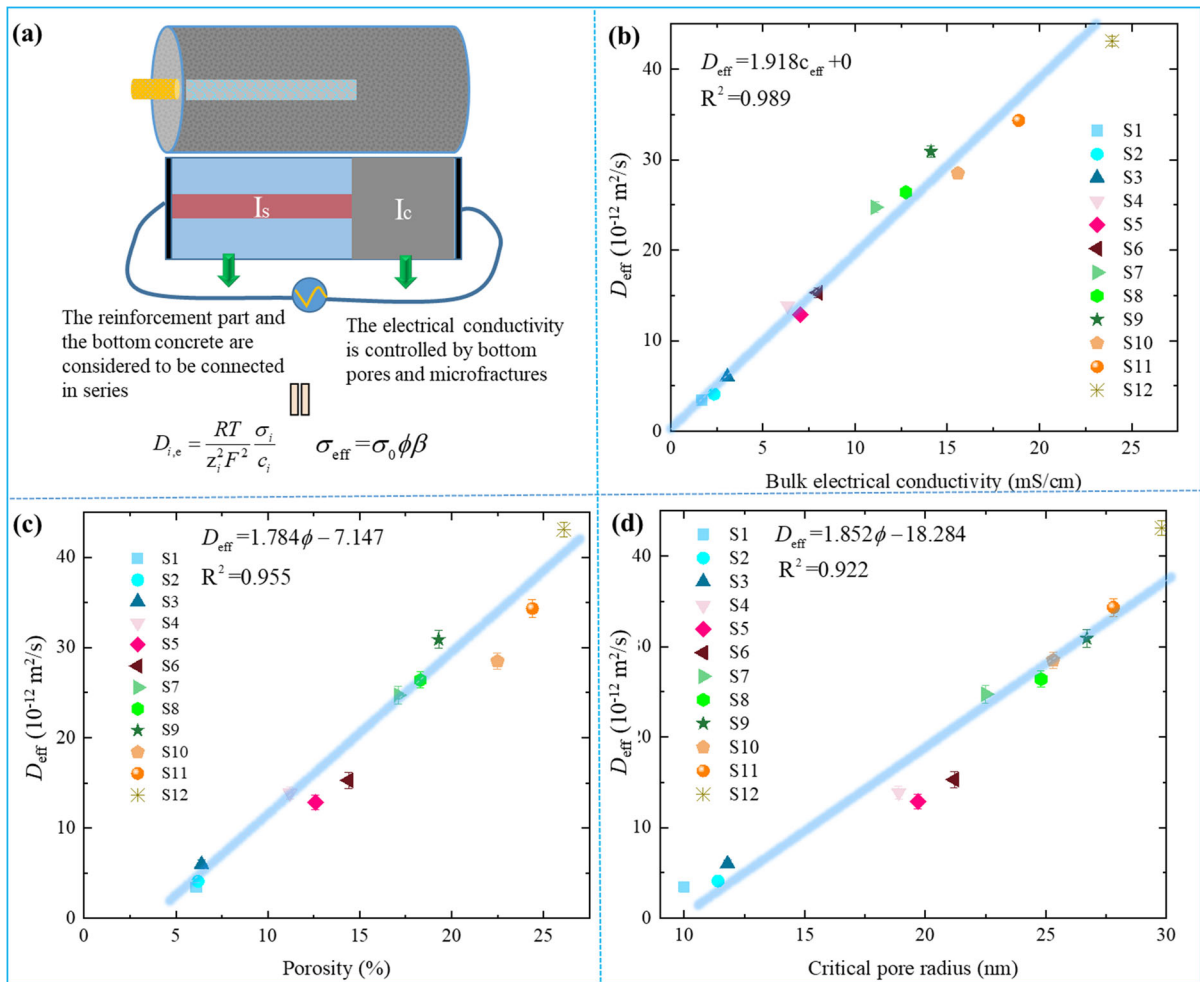


Fig. 9 The correlation between electric conductivity, effective diffusion coefficient and microstructure. **a** schematic diagram of instantaneous electric conductivity test, **b** the correlation between the instantaneous bulk electric conductivity of concrete

and the effective diffusion coefficient (D_{eff}) of chloride, **c** the correlation between effective diffusion coefficient (D_{eff}) of chloride and porosity, **d** the correlation between effective diffusion coefficient (D_{eff}) of chloride and critical pore radius

electrical potential, F the Faraday’s number, R the gas constant, and T the absolute temperature).

The chloride migration caused by concentration diffusion and hydraulic pressure will lead to the change of electrical conductivity in concrete, which will be reflected in the voltage change in constant current induced corrosion. Furthermore, for concrete materials, the error caused by ignoring the non-ideality of chloride solution is very small (i.e. NT Build 355 [38] assumes that the solution is an ideal solution). Therefore, Nernst Planck equation can be reorganized as:

$$D_{i,e} = \frac{J_{i,e} RT}{c_i} \frac{l}{F \Delta E} \tag{8}$$

where l represents the thickness of the sample, ΔE represents the instantaneous voltage drop through the specimen.

Concrete can be regarded as a solid electrolyte [39], For deep burial conditions, the humidity is constant, thus Eq. (8) can also be transformed into Eq. (9).

$$D_{i,e} = \frac{RT}{z_i^2 F^2} \frac{\sigma_i}{c_i} \tag{9}$$

Previous researchers found that the formation factor F_f was related to the charge passed, and



different chloride ion penetration resistance of concrete could be graded according to the equivalent F_f value [40]. Therefore, the formation factor F_f could be related to the description of porous networks. For example, the correlation between the formation factor, the pore connectivity (β) and the porosity tortuosity parameter τ : $F_f = \tau/\varphi$ ($\beta = 1/\varphi$) [37, 38].

It can be seen from Fig. 9b that the correlation between the bulk electric conductivity of concrete and the effective diffusion coefficient (D_{eff}) of chloride, and the fitting relationship was a positive proportion function (passing through the origin point). Further, the effective diffusion coefficient was taken as a dependent variable, the porosity and critical pore size were taken as independent variables with the aim to find general relationships between D_{eff} and microstructure features. The fitting relationships are plotted in Fig. 9c, d. It can be expected that for each specimen, the increase of porosity will lead to more flow paths of chloride ions, further leading to the increase of chloride diffusion coefficient. As shown in Eqs. (5) and (6), the bulk electric conductivity of the specimens were related to the pore networks in the concrete, so that the formation factor F_f and the pore connectivity parameter β of the microstructure in the concrete could be further characterized through the measurement of porosity and electric conductivity of pore solution (see Fig. 10a, b).

Based on the above analysis, under the coupling environment of stray current and high hydraulic pressure, the instantaneous electrical conductivity can well reflect the evolution of the internal microstructure parameters of concrete and the effective diffusion coefficient of chloride ions. On the one hand, corrosive chloride ions were more accessible to micropores with the action of stray current [16, 17], so the migration of chloride ions can adapt to the change of pore shapes. On the other hand, the ultra-deep buried RC structures would be under the groundwater level for a long time, and can be considered as fully saturated. Therefore, there was no measurement fluctuation caused by humidity change [41].

Instantaneous electric conductivity provides an excellent indicator for evaluating chloride diffusion: (1) The measurement of bulk electric conductivity does not require sawing the cement-based composites; (2) The measurement of electric conductivity can realize continuous monitoring, so it is very suitable for early warning indicators; (3) The relationship between electric conductivity and diffusion coefficient has clear physical significance.

5.2 Deterioration mechanism and model

The deterioration mechanism was obtained from FTIR, Vickers hardness, computer tomography and pull-out tests. The FTIR study of chemical bonds and

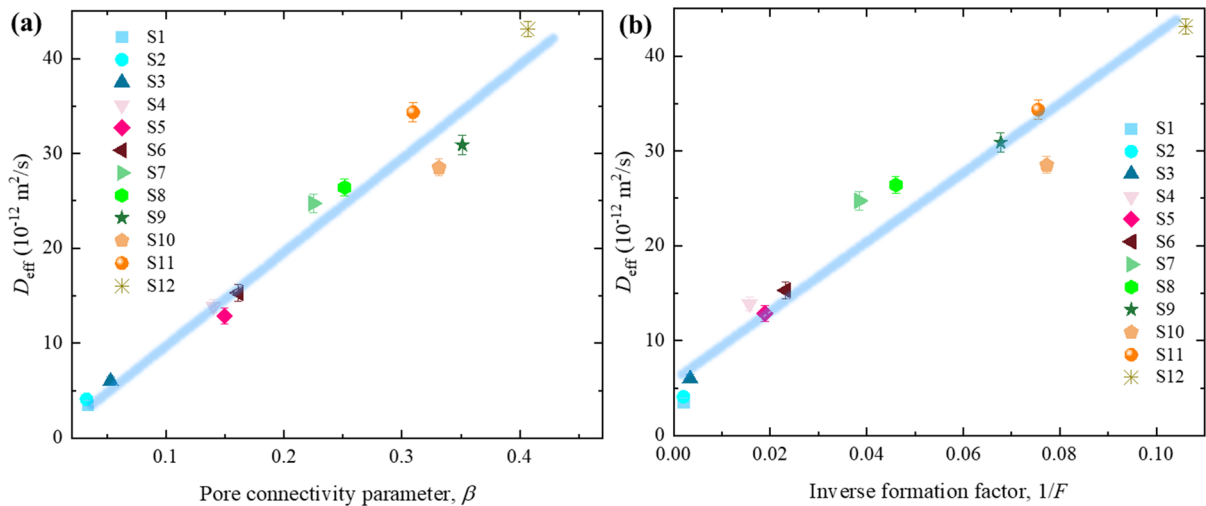


Fig. 10 The correlation between effective diffusion coefficient of chloride and the microstructure characteristics. **a** the correlation between effective diffusion coefficient (D_{eff}) of

chloride and pore connectivity parameter (β), **b** the correlation between effective diffusion coefficient (D_{eff}) of chloride and inverse formation factor ($1/F$)

functional groups in cement matrix provided a reasonable explanation for the Vickers hardness test results: the weakening of the signal peaks of these chemical bonds represented the leaching of corresponding cement hydration products, which also led to the decline of concrete strength. According to Eq. (3), as an index obtained from bearing capacity deformation data, Vickers hardness has been widely used as an excellent indicator to describe local strength, and its linear fitting with concrete strength has a very high confidence [42, 43]. The interaction and roughness of interfaces between different materials have also been used for modeling by other researches [44, 45].

The theoretical bond-slip curves are piecewise functions, and the engineering design mainly focuses on the first two stages: shear dilatancy of stage I and progressive failure of stage II. As show in Fig. 11a (the original experimental data), the initially loaded part experienced a slip with almost no increase in bond stress. Considering the contact gap between the loading frame and the specimen as shown in Fig. 11b, this part is not considered in the bond-slip model. The gap value between the rigid frame and the specimen was determined by the following method: the linear

segment in the experimental bond-slip curves was considered the elastic stage (e.g. the black linear segment in Fig. 11b), the starting point of the linear stage was considered the value of the contact gap, and the endpoint of the linear stage was considered the starting point of stage II. The non-corroded reinforcement could be simplified into a series of regular rough bodies because the transverse ribs and longitudinal ribs recurred quite regularly (see Fig. 12a). The corrosion induced by stray current made the concrete around the reinforcement suffer from leaching deterioration, so larger thickness of ITZ appeared (S4–S12). Figure 12b is the schematic diagram of geometric quantification of the rough interface before and after corrosion to analyze the mechanism of the change of bond stress. CT scanning was used to obtain the outline of the corroded rebar and the distribution of rust. The rough interfaces were replaced by a series of isosceles trapezoids of different heights. The corroded part was represented by an isosceles trapezoid with reduced height to indicate the weakened contact with the concrete, which was obtained by subtracting the size contour of the corroded reinforcement from the size of the non-corroded reinforcement.

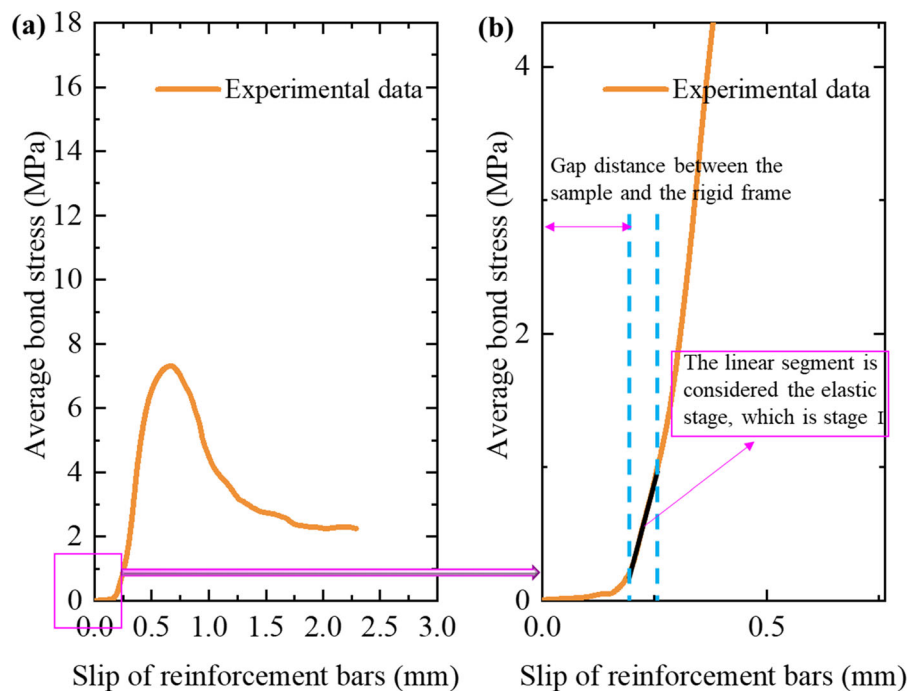


Fig. 11 Method for determining the elastic stage and determining the contact gap



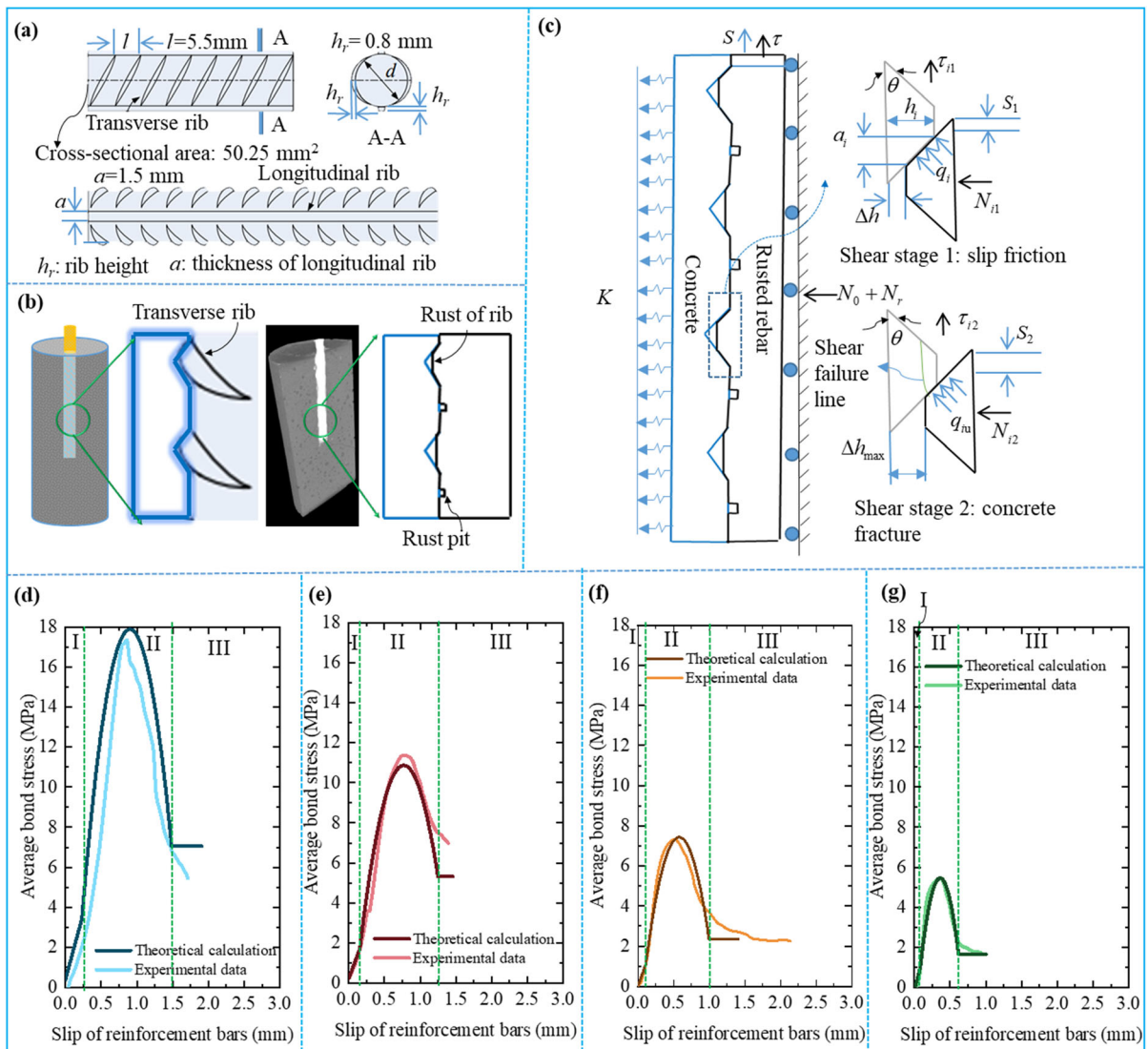


Fig. 12 Prediction of degraded bonding stress. **a** regular distribution of transverse and longitudinal ribs of the reinforcement before the corrosion test, **b** the schematic diagram of geometric quantification of the rough interface before and after corrosion, **c** mechanical analysis model of bond-slip progressive

failure between corroded reinforcement and concrete, **d, e, f** and **g** comparison between theoretical calculation and experimental data of representative specimens S1, S4, S7, S10 (stage I: shear dilatancy, stage II: progressive failure, stage III: residual stress)

The conceptual model is shown in Fig. 12c. The overall shear response of the interface between reinforcement and concrete can be obtained by summing the shear responses of all individual local rough bodies [46]. The calculation method is as follows:

$$\tau A = \sum_{i=1}^n a_i N_i \mu_i \tag{10}$$

where A is the nominal area of the interface, a_i, N_i and μ_i are the contact projection area, normal stress and friction coefficient of a local single rough body respectively. Equation (10) can be simplified into two-dimensional analysis, and the nominal area of the

contact surface can be simplified into the nominal length of the contact line.

$$\tau L = \sum_{i=1}^n a_i N_i \mu_i \tag{11}$$

According to the geometric relationship in Fig. 12c, Eq. (12) can be obtained

$$a_i = \frac{h_i}{\tan(\theta)} - S \tag{12}$$

where S is the shear (sliding) displacement.

The local normal stress on the interface can be obtained as follows:

$$N_i = \frac{2h_i [N_0 + N_r + KS \tan(\theta)]}{a_i \tan(\theta)} \tag{13}$$

where, N_0 is the initial normal stress, and N_r is the normal stress caused by corrosion of reinforcement. K is the normal restraint stiffness.

With simultaneous Eqs. (10)–(13), the overall bond (shear) stress and strain expression of the interface can be obtained as follows:

$$\tau = \frac{1}{L} \sum_{i=1}^n 2 \frac{h_i [N_0 + N_r + KS \tan(\theta)] \mu_i}{\tan(\theta)} \tag{14}$$

It can be seen from Eq. (14) that determining the friction coefficient between the corroded reinforcement and concrete is the key to solving the shear response of local rough bodies, and the overall bond-slip curve can be obtained by summing the shear-slip of local rough bodies.

As shown in Fig. 12c, the shear process includes two stages, the first stage is the friction shear dilatancy stage, the second stage is the shear fracture stage. Consistent with the practice of Luo et al. [46]. For the solution of stage II, the ultimate bearing capacity of rough body, q_{iu} , is obtained by using the slip-line field theory as [47, 48]:

$$q_{iu} = c \tan(\varphi) \left[\frac{1 + \sin(\varphi)}{1 - \sin(\varphi)} \exp(\pi - 4\theta) \tan(\varphi) - 1 \right] \tag{15}$$

where c and φ are the cohesion and friction angle of concrete with weakened strength under different stray currents and high hydraulic pressure coexistence environment.

According to the static equilibrium condition of the local rough body in the critical state (see Fig. 12c).

$$Q_{iu} = \frac{2h_i [\sigma_0 + \sigma_r + KS_i^c \tan(\theta)] [\cos(\theta) + \tan(\theta + \varphi_b) \sin(\theta)]}{h_i - S_i^c \tan(\theta)} \tag{16}$$

where S_i^c is the critical shear displacement, φ_b is the basic internal friction angle.

Strength index was obtained by establishing the correlation between Vickers hardness and strength, similar to previous studies [42, 43]. To solve the bond-slip curves, it is necessary to determine the normal stiffness K , which represents the lateral dilatancy slip at the interface between reinforcement and concrete under vertical load. According to the expansion theory of circular hole, the normal stiffness K can be solved by Eq. (17).

$$K = \frac{E_r}{r(1 + \nu_r)} \tag{17}$$

where E_r , ν_r is the elastic modulus of concrete and Poisson's ratio of concrete; r is the radius of reinforcement.

The slope of the linear stage is the value of the elastic modulus. Therefore, the weakening of E_r in the elastic stage (stage I) due to the influence of stray currents and water pressure was considered. the interaction relationship between the elastic modulus value obtained through the linear segment, the stray current and water pressure was established:

$$E_r = 3.457 - 1.237 \cdot SC - 0.103 \cdot WP - 0.276 \cdot SC \cdot WP \tag{18}$$

where E_r represents the elastic modulus ($\times 10^4$ MPa), SC is the value (A/m^2) of stray current, WP is the value (MPa) of hydraulic pressure. The correlation coefficient (r^2) is 0.962 for E_r , indicating that the model fit the experimental data well.

The comparison between theoretical calculation results and experimental data is shown in Figs. 12d–g, and it can be seen that the current model is consistent with the results of Vickers hardness test and previous studies [49, 50]. Considering the contact gap between the rigid frame and the specimen, as well as the weakened elastic modulus, the proposed model has good prediction accuracy. The establishment of constitutive equation based on interface morphology and



roughness has been proved to be a good meso-modeling approach [44, 45, 51, 52].

5.3 Engineering implications

The current research has significant theoretical and practical implications. Considering the characteristics of deep underground spaces with constant humidity, the physical relationship between bulk electric conductivity, effective diffusion coefficient, and internal microstructure (i.e., the “paths” for chloride ions diffusion) of concrete was derived and verified. The instantaneous electric conductivity method could accurately characterize the degree of ion diffusion and had a good correlation with the pore structure. Additionally, a bond-slip degradation model was constructed at a meso-scale, and verified with macroscopic pull-out test. Thus, current model started from the essence of the degradation mechanism under stray current and high hydraulic pressure coexistence environment, rather than establishing phenomenological models to fit the experimental curves [53, 54]. Therefore, the present research provides a powerful new tool for predicting the mechanical properties of corroded reinforced concrete in ultra-deep underground space of coastal cities.

6 Conclusion

The development of ultra-deep underground spaces (40 m–100 m) in coastal megacities has been put on the agenda. However, the chloride induced corrosion of reinforced concrete (RC) under stray current and high hydraulic pressure coexistence environment remains an urgent issue to be addressed. To tackle this problem, a novel experimental system was developed. The instantaneous electric conductivity evolution of RC was continuously monitored throughout the whole deterioration process. Furthermore, the microstructure of concrete near the reaction surfaces, physical and mechanical properties related to the interface transition zone (ITZ) between corroded reinforcement and concrete, and the pullout resistance of the deteriorated specimens were comprehensively analyzed. Based on the comprehensive experimental research and theoretical analysis, a new evaluation method of chloride diffusion and the mechanism of bond deterioration of corroded reinforced concrete in

an ultra-deep buried environment were obtained. The main conclusions are as follows:

1. Due to electrochemical decomposition, the larger the stray current, the more micropores would be obtained. The action of high hydraulic pressure was mainly reflected in macropores. With the increase of hydraulic pressure, the proportion of macropores increased.
2. The instantaneous electrical conductivity can reflect the microstructure characteristics of pores in concrete (the “paths” for chloride diffusion). Stray current promotes the accessibility of ions, thus improving the conductivity of concrete. The physical relationship between the bulk electric conductivity of concrete and the effective diffusion coefficient of chloride ions as well as the internal microstructure of concrete has been derived and verified.
3. Vickers hardness test is a reliable method to indirectly evaluate the thickness of ITZ, and the Vickers hardness test results have the same evolution law as the microstructure of concrete: the strength deterioration of concrete was mainly affected by stray current, and the stray current was not only the deterioration of ITZ, but also showed a significant reduction in microhardness at all test points.
4. The ultimate bond stress decreased with the increase of stray current and hydraulic pressure. FTIR was used to predict the molecular structure characteristics of deteriorated concrete. In addition, CT scanning was used to model the rough bodies and Vickers hardness was used to model the mechanical indicators. Finally, a bond stress degradation model was established, which was a reliable way to evaluate the bond strength of corroded RC.

Acknowledgements This work was supported by the State Major Program of National Natural Science Foundation of China (Grant Number 52090082); National Natural Science Foundation of China (Grant Number 51808207); High-level Talent of Innovative Research Team of Hunan Province, China (2019RS1030).

Author contributions Conceptualization: [YC, XK]; Methodology: [YC, XK]; Formal analysis and investigation: [YC, XK, RC]; writing—original draft preparation: [YC, MC]; writing—review and editing: [YC, XK, RC, MC]; funding



acquisition: [XK, RC]; Resources: [YC, MC]; Supervision: [XK, RC].

Data availability The datasets generated during the current study are available from the corresponding author on reasonable request.

Declarations

Conflict of interest The authors declare that they have no known competing financial interests or personal relationships that could have appeared to influence the work reported in this paper.

References

- Kazemi H, Yekrangnia M, Shakiba M et al (2023) Bond durability between anchored GFRP bar and seawater concrete under offshore environmental conditions. *Mater Struct* 56:64. <https://doi.org/10.1617/s11527-023-02153-5>
- Castañeda-Valdés A, Corvo F, Marrero-Águila R et al (2023) The service life of reinforced concrete structures in an extremely aggressive coastal city. Influence of concrete quality. *Mater Struct* 56:12. <https://doi.org/10.1617/s11527-023-02100-4>
- Mastrocicco M, Colombani N (2021) The issue of groundwater salinization in coastal areas of the mediterranean region: a review. *Water (Switzerland)* 13(1):90. <https://doi.org/10.3390/w13010090>
- Vetrimurugan E, Elango L, Rajmohan N (2013) Sources of contaminants and groundwater quality in the coastal part of a river delta. *Int J Environ Sci Technol* 10:473–486. <https://doi.org/10.1007/s13762-012-0138-3>
- Zhang XH, Wang XW, Xu YS (2022) Groundwater environment and related potential engineering disasters of deep underground space in Shanghai. *Bull Eng Geol Environ* 81:203. <https://doi.org/10.1007/s10064-022-02692-1>
- Luo CY, Shen SL, Han J et al (2015) Hydrogeochemical environment of aquifer groundwater in Shanghai and potential hazards to underground infrastructures. *Nat Hazards* 78:753–774. <https://doi.org/10.1007/s11069-015-1172-5>
- Xu SY, Li W, Wang YQ (2013) Effects of vehicle running mode on rail potential and stray current in DC mass transit systems. *IEEE Trans Veh Technol* 62:3569–3580. <https://doi.org/10.1109/TVT.2013.2265093>
- Bertolini L, Carsana M, Pedferri P (2007) Corrosion behaviour of steel in concrete in the presence of stray current. *Corros Sci* 49:1056–1068. <https://doi.org/10.1016/j.corsci.2006.05.048>
- Zhao Y, Lin H, Wu K, Jin W (2013) Bond behaviour of normal/recycled concrete and corroded steel bars. *Constr Build Mater* 48:348–359. <https://doi.org/10.1016/j.conbuildmat.2013.06.091>
- Ming J, Zhou X, Zuo H et al (2022) Effects of stray current and silicate ions on electrochemical behavior of a high-strength prestressing steel in simulated concrete pore solutions. *Corros Sci* 197:110083. <https://doi.org/10.1016/j.corsci.2022.110083>
- Chen MY, Chen RP, Chen YQ et al (2023) Stray current induced chloride ion transport and corrosion characteristics of cracked ultra-high performance concrete. *Constr Build Mater* 398:125618. <https://doi.org/10.1016/j.conbuildmat.2023.132536>
- Wu P, Zhu X, Xu L et al (2020) Effect of stray current coupled with chloride concentration and temperature on the corrosion resistance of a steel passivation film. *Electrochem Commun* 118:106793. <https://doi.org/10.1016/j.elecom.2020.106793>
- Machner A, Bjørndal M, Šajna A et al (2022) Impact of leaching on chloride ingress profiles in concrete. *Mater Struct* 55:8. <https://doi.org/10.1617/s11527-021-01730-w>
- Gérard B, Le Bellego C, Bernard O (2002) Simplified modelling of calcium leaching of concrete in various environments. *Mater Struct* 35:632–640. <https://doi.org/10.1007/BF02480356>
- Cai X, He Z, Shao Y, Sun H (2016) Macro- and micro-characteristics of cement binders containing high volume fly ash subject to electrochemical accelerated leaching. *Constr Build Mater* 116:25–35. <https://doi.org/10.1016/j.conbuildmat.2016.02.059>
- Chen YQ, Ma XY, Tong XY, Kang X (2023) Microstructures evolution and chloride migration characteristics of concrete under ultra-deep underground environment. *Cem Concr Compos* 137:104936. <https://doi.org/10.1016/j.cemconcomp.2023.104936>
- Chen YQ, Chen MY, Tong XY, Wang SQ, Kang X (2022) Molecular insights into the interactions between chloride liquids and C-S-H nanopore surfaces under electric field-induced transport. *J Mol Liq* 274:119942. <https://doi.org/10.1016/j.molliq.2022.119942>
- Chen YQ, Wang SQ, Tong XY, Kang X (2022) Towards the sustainable fine control of microbially induced calcium carbonate precipitation. *J Clean Prod* 377:134395. <https://doi.org/10.1016/j.jclepro.2022.134395>
- Ojeda ML, Esparza JM, Campero A et al (2003) On comparing BJH and NLDFT pore-size distributions determined from N₂ sorption on SBA-15 substrata. *Phys Chem Chem Phys* 5:1859–1866. <https://doi.org/10.1039/b300821e>
- Krakowiak JK, Wilson W, James S et al (2015) Inference of the phase-to-mechanical property link via coupled X-ray spectrometry and indentation analysis: application to cement-based materials. *Cem Concr Res* 67:271–285. <https://doi.org/10.1016/j.cemconres.2014.09.001>
- Standards IT (2002) Overview of mechanical testing standards. CSM Instruments, Needham Heights
- Chen YQ, Wang SQ, Tong XY et al (2022) Crystal transformation and self-assembly theory of microbially induced calcium carbonate precipitation. *Appl Microbiol Biotechnol* 106:3555–3569. <https://doi.org/10.1007/s00253-022-11938-7>
- Phung QT, Maes N, Jacques D et al (2016) Modelling the evolution of microstructure and transport properties of cement pastes under conditions of accelerated leaching. *Constr Build Mater* 115:179–192. <https://doi.org/10.1016/j.conbuildmat.2016.04.049>
- Zhang EQ, Abbas Z, Tang L (2018) Predicting degradation of the anode–concrete interface for impressed current



- cathodic protection in concrete. *Constr Build Mater* 185:57–68. <https://doi.org/10.1016/j.conbuildmat.2018.07.025>
25. Thommes M, Kaneko K, Neimark AV et al (2015) Physisorption of gases, with special reference to the evaluation of surface area and pore size distribution (IUPAC Technical Report). *Pure Appl Chem* 87:1051–1069. <https://doi.org/10.1515/pac-2014-1117>
26. Han S, Kwak D, Lee Y et al (2017) Relative permeability prediction considering complex pore geometry and wetting characteristics in carbonate reservoirs. *Int J Oil Gas Coal T* 15:331–346. <https://doi.org/10.1504/IJOGCT.2017.084836>
27. Leung Tang P, Alqassim M, Nic Daéid N et al (2016) Nondestructive Handheld Fourier Transform Infrared (FT-IR) analysis of spectroscopic changes and multivariate modeling of thermally degraded plain Portland cement concrete and its slag and fly ash-based analogs. *Appl Spectrosc* 70:923–931. <https://doi.org/10.1177/0003702816638306>
28. Horgnies M, Chen JJ, Bouillon C (2013) Overview about the use of fourier transform infrared spectroscopy to study cementitious materials. *WIT Trans Eng Sci* 77:251–262. <https://doi.org/10.2495/MC130221>
29. Trezza MA, Lavat AE (2001) Analysis of the system $3\text{CaO}\cdot\text{Al}_2\text{O}_3\text{-CaSO}_4\cdot 2\text{H}_2\text{O}\text{-CaCO}_3\text{-H}_2\text{O}$ by FT-IR spectroscopy. *Cem Concr Res* 31:869–872. [https://doi.org/10.1016/S0008-8846\(01\)00502-6](https://doi.org/10.1016/S0008-8846(01)00502-6)
30. Jose A, Nivitha MR, Krishnan JM, Robinson RG (2020) Characterization of cement stabilized pond ash using FTIR spectroscopy. *Constr Build Mater* 263:120136. <https://doi.org/10.1016/j.conbuildmat.2020.120136>
31. Nasrazadani S, Eghtesad R, Sudoi E et al (2016) Application of Fourier transform infrared spectroscopy to study concrete degradation induced by biogenic sulfuric acid. *Mater Struct* 49:2025–2034. <https://doi.org/10.1617/s11527-015-0631-5>
32. Sola E, Özbolt J, Balabanić G, Mir ZM (2019) Experimental and numerical study of accelerated corrosion of steel reinforcement in concrete: Transport of corrosion products. *Cem Concr Res* 120:119–131. <https://doi.org/10.1016/j.cemconres.2019.03.018>
33. Dong B, Fang G, Liu Y et al (2017) Monitoring reinforcement corrosion and corrosion-induced cracking by X-ray microcomputed tomography method. *Cem Concr Res* 100:119–131. <https://doi.org/10.1016/j.cemconres.2017.07.009>
34. Wong HS, Zhao YX, Karimi AR et al (2010) On the penetration of corrosion products from reinforcing steel into concrete due to chloride-induced corrosion. *Corros Sci* 52:2469–2480. <https://doi.org/10.1016/j.corsci.2010.03.025>
35. Gallé C (2001) Effect of drying on cement-based materials pore structure as identified by mercury intrusion porosimetry—a comparative study between oven-, vacuum-, and freeze-drying. *Cem Concr Res* 31:1467–1477. [https://doi.org/10.1016/S0008-8846\(01\)00594-4](https://doi.org/10.1016/S0008-8846(01)00594-4)
36. Sanish KB, Neithalath N, Santhanam M (2013) Monitoring the evolution of material structure in cement pastes and concretes using electrical property measurements. *Constr Build Mater* 49:288–297. <https://doi.org/10.1016/j.conbuildmat.2013.08.038>
37. Andrade C (1993) Calculation of chloride diffusion coefficients in concrete from ionic migration measurements. *Cem Concr Res* 23:724–742. [https://doi.org/10.1016/0008-8846\(93\)90023-3](https://doi.org/10.1016/0008-8846(93)90023-3)
38. NT BUILD 355 (1997) Concrete, mortar and cement based repair materials: Chloride diffusion coefficient from migration cell experiments. Nordtest Build
39. Lu X (1997) Application of the Nernst-Einstein equation to concrete. *Cem Concr Res* 27:293–302. [https://doi.org/10.1016/S0008-8846\(96\)00200-1](https://doi.org/10.1016/S0008-8846(96)00200-1)
40. Ann KY, Hong SI (2018) Modeling chloride transport in concrete at pore and chloride binding. *ACI Mater J* 115:595–604. <https://doi.org/10.14359/51702194>
41. Smyl D (2020) Electrical tomography for characterizing transport properties in cement-based materials: a review. *Constr Build Mater* 244:118299
42. Chu H, Wang T, Han L et al (2021) Vickers hardness distribution and prediction model of cement pastes corroded by sulfate under the coexistence of electric field and chloride. *Constr Build Mater* 309:125119. <https://doi.org/10.1016/j.conbuildmat.2021.125119>
43. Jiang C, Jiang L, Tang X et al (2021) Impact of calcium leaching on mechanical and physical behaviors of high belite cement pastes. *Constr Build Mater* 286:122983. <https://doi.org/10.1016/j.conbuildmat.2021.122983>
44. Ma XY, Lei H, Xin K (2023) Examination of interface roughness and particle morphology on granular soil–structure shearing behavior using DEM and 3D printing. *Eng Struct* 290:116365. <https://doi.org/10.1016/j.engstruct.2023.116365>
45. Ma XY, Lei H, Kang X (2022) Effects of particle morphology on the shear response of granular soils by discrete element method and 3D printing technology. *Int J Numer Anal Methods Geomech* 46:2191–2208. <https://doi.org/10.1002/nag.3384>
46. Luo Q, Wang W, Wang B et al (2021) Numerical study on interface optimization of new-to-old concrete with the slant grooves. *Structures* 34:381–399. <https://doi.org/10.1016/j.istruc.2021.07.094>
47. Freddi F, Royer-Carfagni G (2016) Phase-field slip-line theory of plasticity. *J Mech Phys Solids* 94:257–272. <https://doi.org/10.1016/j.jmps.2016.04.024>
48. Tapponnier P, Molnar P (1976) Slip-line field theory and large-scale continental tectonics. *Nature* 264:319–324. <https://doi.org/10.1038/264319a0>
49. Li Y, Liu Y, Wang R (2021) Evaluation of the elastic modulus of concrete based on indentation test and multi-scale homogenization method. *J Build Eng* 43:102758. <https://doi.org/10.1016/j.jobe.2021.102758>
50. Velez K, Maximilien S, Damidot D et al (2001) Determination by nanoindentation of elastic modulus and hardness of pure constituents of Portland cement clinker. *Cem Concr Res* 31:555–561. [https://doi.org/10.1016/S0008-8846\(00\)00505-6](https://doi.org/10.1016/S0008-8846(00)00505-6)
51. Chen YQ, Wen CP, Fang XQ (2019) Modified Yin’s double-yield-surface model for bioenzyme-treated expansive soil. *Yantu Lixue/Rock Soil Mech* 40:3515–3523. <https://doi.org/10.16285/j.rsm.2018.1004>
52. Chen YQ, Wen CP, Fang XQ et al (2019) Stress-strain relationships of bioenzyme-treated expansive soil. *J Central*



- South Univ Sci Technol 50:1981–1990. <https://doi.org/10.11817/j.issn.1672-7207.2019.08.026>
53. Feng Q, Visintin P, Oehlers DJ (2016) Deterioration of bond-slip due to corrosion of steel reinforcement in reinforced concrete. *Mag Concr Res* 68:00217. <https://doi.org/10.1680/jmacr.15.00217>
54. Jiang C, Wu YF, Dai MJ (2018) Degradation of steel-to-concrete bond due to corrosion. *Constr Build Mater* 158:1073–1080. <https://doi.org/10.1016/j.conbuildmat.2017.09.142>

Publisher's Note Springer Nature remains neutral with regard to jurisdictional claims in published maps and institutional affiliations.

Springer Nature or its licensor (e.g. a society or other partner) holds exclusive rights to this article under a publishing agreement with the author(s) or other rightsholder(s); author self-archiving of the accepted manuscript version of this article is solely governed by the terms of such publishing agreement and applicable law.

